



# Automatic Lung Cancer Segmentation in [<sup>18</sup>F]FDG PET/CT Using a Two-Stage Deep Learning Approach

Junyoung Park<sup>1,2</sup> · Seung Kwan Kang<sup>2,3,4,5</sup> · Donghwi Hwang<sup>2,3,4</sup> · Hongyoon Choi<sup>2</sup> · Seunggyun Ha<sup>6</sup> · Jong Mo Seo<sup>1</sup> · Jae Seon Eo<sup>7</sup> · Jae Sung Lee<sup>2,3,4,5,8</sup> 

Received: 23 September 2021 / Revised: 10 March 2022 / Accepted: 12 March 2022 / Published online: 11 May 2022  
© The Author(s), under exclusive licence to Korean Society of Nuclear Medicine 2022

## Abstract

**Purpose** Since accurate lung cancer segmentation is required to determine the functional volume of a tumor in [<sup>18</sup>F]FDG PET/CT, we propose a two-stage U-Net architecture to enhance the performance of lung cancer segmentation using [<sup>18</sup>F]FDG PET/CT.

**Methods** The whole-body [<sup>18</sup>F]FDG PET/CT scan data of 887 patients with lung cancer were retrospectively used for network training and evaluation. The ground-truth tumor volume of interest was drawn using the LifeX software. The dataset was randomly partitioned into training, validation, and test sets. Among the 887 PET/CT and VOI datasets, 730 were used to train the proposed models, 81 were used as the validation set, and the remaining 76 were used to evaluate the model. In Stage 1, the global U-net receives 3D PET/CT volume as input and extracts the preliminary tumor area, generating a 3D binary volume as output. In Stage 2, the regional U-net receives eight consecutive PET/CT slices around the slice selected by the Global U-net in Stage 1 and generates a 2D binary image as the output.

**Results** The proposed two-stage U-Net architecture outperformed the conventional one-stage 3D U-Net in primary lung cancer segmentation. The two-stage U-Net model successfully predicted the detailed margin of the tumors, which was determined by manually drawing spherical VOIs and applying an adaptive threshold. Quantitative analysis using the Dice similarity coefficient confirmed the advantages of the two-stage U-Net.

**Conclusion** The proposed method will be useful for reducing the time and effort required for accurate lung cancer segmentation in [<sup>18</sup>F]FDG PET/CT.

**Keywords** Lung cancer · Deep learning · Segmentation · PET/CT

✉ Jae Seon Eo  
jaeseon76@gmail.com

✉ Jae Sung Lee  
jaes@snu.ac.kr

Junyoung Park  
parkjun210@snu.ac.kr

Seung Kwan Kang  
kevin.kang@brtnx.com

Donghwi Hwang  
hwang0310@snu.ac.kr

Hongyoon Choi  
chy1000@gmail.com

Seunggyun Ha  
seunggyun.ha@gmail.com

Jong Mo Seo  
callme@snu.ac.kr

## Introduction

Lung cancer is one of the most common types of cancers and is the leading cause of cancer-related deaths in the USA [1] as well as other countries. Optimal and personalized management of lung cancer depends on the histological subtype, molecular characteristics, and tumor stage [2]. [<sup>18</sup>F]fluorodeoxyglucose ([<sup>18</sup>F]FDG) positron emission tomography/computed tomography (PET/CT), which allows visualization of the molecular features and anatomical abnormalities of the target lesion, is considered as an essential medical examination for lung cancer diagnosis and staging. Therefore, many guidelines recommend the use of [<sup>18</sup>F]FDG PET/CT for the evaluation of patients suffering from lung cancer [3–5].

Recently, deep learning algorithms have been actively applied to various tasks in medical image processing

Extended author information available on the last page of the article

and analysis, including lesion and organ detection, segmentation, and image restoration [6–15]. Furthermore, attempts have been made to apply machine learning algorithms to [ $^{18}\text{F}$ ]FDG PET/CT analysis for lung cancer. In particular, various studies have been conducted to improve lesion detectability and predict the characteristics of the lesions [16–19]. Furthermore, accurate tumor segmentation is required to determine the functional volume of tumors in PET/CT [20]. However, studies related to improving the accuracy of tumor segmentation are limited [21].

U-Net [22] is one of the most widely used deep learning networks for medical image segmentation [23–26]. The deeply supervised encoder–decoder network, which crops and copies feature maps from the encoding units to the decoding units, processes the entire image in the forward pass to directly generate the segmentation maps [27, 28]. The two-dimensional (2D) U-Net, which converts 2D image slices into 2D slices, is simple and fast, but occasionally introduces discontinuity artifacts while stacking 2D network outputs to generate three-dimensional (3D) volume [29]. The discontinuity artifacts can be mitigated by employing 3D U-Nets [30]. However, they are computationally expensive and require a considerable computer memory. Therefore, the limited computation resources, which are generally used to process the large 3D datasets, would lead to suboptimal network architecture and training.

Therefore, in this study, we propose a two-stage U-Net architecture to enhance the lung cancer segmentation performance in FDG PET/CT. In this method, a global 3D U-Net that may be suboptimal for the given task is applied to select the candidate lung cancer regions, and 2.5D U-Net, which is a compromise between the 2D and 3D U-Nets and employs a multislice input, is applied for the final lung cancer segmentation. In the following sections, the details of the two-stage U-Net architecture and its training and testing methods are described.

## Materials and Methods

### Datasets

The whole-body [ $^{18}\text{F}$ ]FDG PET/CT scan data of 887 patients with lung cancer were retrospectively used for network training and evaluation. The retrospective use of the scan data and waiver of consent were approved by the institutional review board of our institution. The patients fasted for at least 6 h prior to image acquisition, resulting in blood glucose levels that were  $< 140$  mg/dL. [ $^{18}\text{F}$ ]FDG (5.18 MBq/kg) was injected intravenously into the patients, and PET scans were performed 60 min post injection using Biograph mCT40 or mCT64 PET/CT scanners (Siemens Healthineers, Knoxville, TN). The PET scan data were obtained from the base of the skull to the proximal thigh, followed by a CT scan obtained for attenuation correction and anatomical localization. PET images were reconstructed using an iterative algorithm (ordered-subset expectation maximization, iteration number 2 and 21 subsets) with an image matrix size of  $200 \times 200 \times \sim 200$  and voxel size of  $2.43 \times 2.43 \times 4.95$  mm $^3$ . The size of the reconstructed CT images was  $512 \times 512 \times \sim 490$  ( $0.98 \times 0.98 \times 2.0$  mm $^3$ ).

Ground-truth tumor volume-of-interests (VOIs) were drawn semi-automatically [31] using the LifeX software (<https://www.lifexsoft.org/>, version 4.0) [32]. Spherical VOIs were manually drawn on the PET images to include the primary tumor lesions; the metabolically active tumor regions in the spherical VOI were segmented by applying an adaptive threshold depending on the tumor and background intensities [33].

The dataset was randomly partitioned into training, validation, and test sets. Among the 887 PET/CT and VOI datasets, 730 were used to train the proposed models, 81 were used as the validation set, and the remaining 76 were used to evaluate the model.

Prior to network training and evaluation, the image size was adjusted because the voxel sizes and dimensions of the

**Fig. 1** Two-stage U-Net architecture

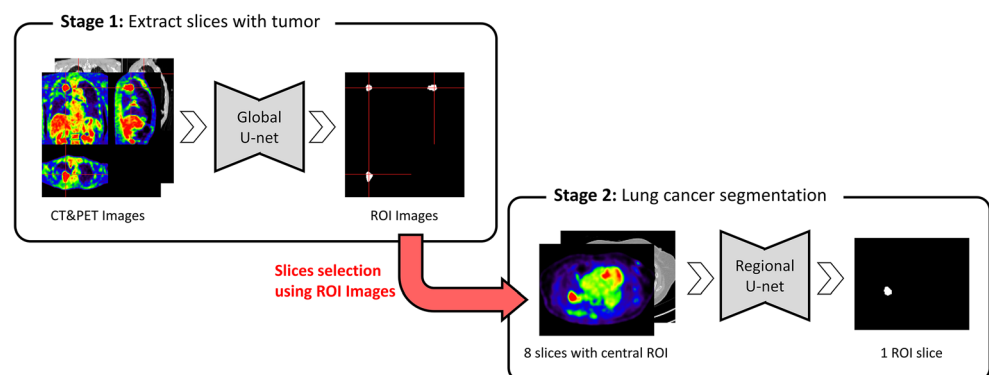
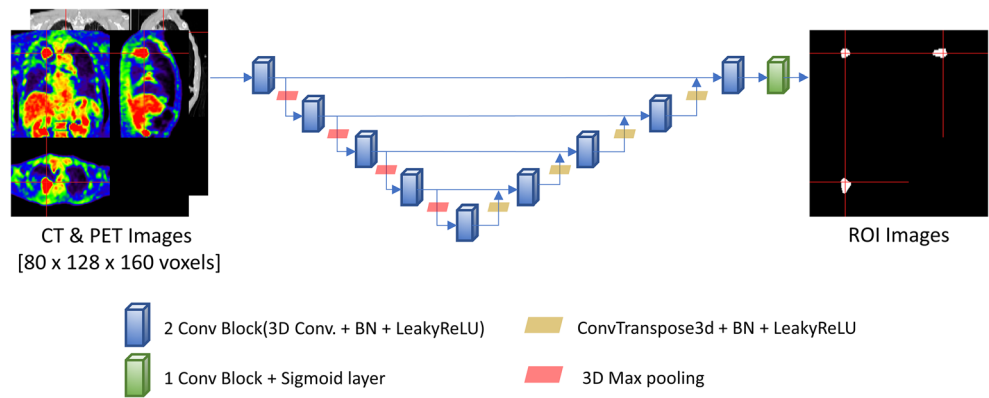


**Fig. 2** Global 3D U-Net in Stage 1



PET and CT images were different. Because the VOIs for the primary tumor were segmented from the PET images, the images and voxel sizes of the CT images matched well with those of the PET images using trilinear interpolation.

**Model Architecture**

As described earlier, we designed a two-stage U-Net architecture to enhance the tumor segmentation performance (Fig. 1). In Stage 1, a global U-Net receives 3D PET/CT volume as the input and extracts the preliminary tumor area, thus generating a 3D binary volume as the output. In Stage 2, a regional U-Net receives eight consecutive PET/CT slices around the slice selected by the Global U-net in Stage 1 and generates a 2D binary image as the output.

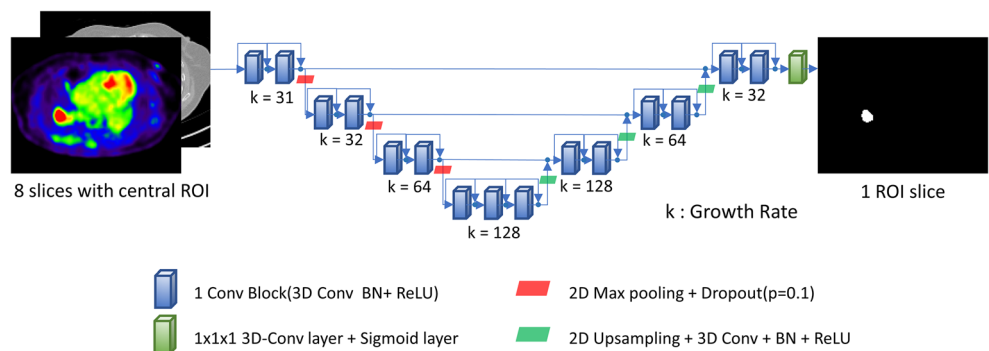
Figure 2 shows the detailed structure of the global U-Net used in Stage 1. We designed the detailed structure of Global U-Net based on a 3D U-Net [30] that demonstrated good performance in our previous works [23, 24, 34–36]. Rather than using the classification model, a segmentation model was used in stage 1. If a slice is included in the 3D tumor volume that Global U-Net produces, the index of slice is passed onto Stage 2, where the regional U-Net that will be described in the next section was applied for the final lung cancer segmentation.

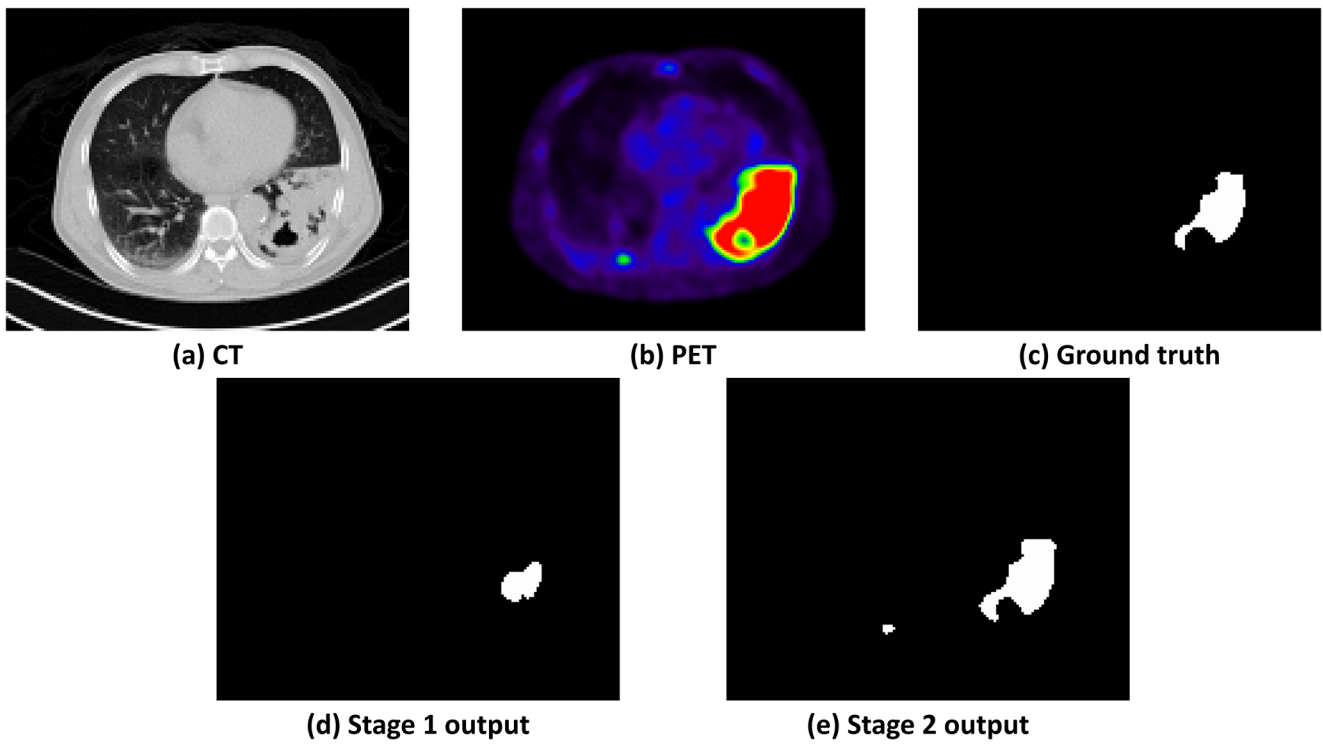
To reduce the learning time and memory consumption, the PET/CT images were cropped to have dimensions of  $80 \times 128 \times 160$  with a focus on the lungs. The initial convolution block comprised six channels, thus providing twice the number of channels for each down-sampling. The contracting path comprised two convolutional blocks. Each convolution block comprised  $3 \times 3 \times 3$  convolution layers, with batch normalization and leakyReLU with a negative slope of 0.2 as an activation function. In addition, a  $2 \times 2 \times 2$  max pooling operation with stride 2 was used for down-sampling. In the extracting path, the number of channels was reduced by 1/3 after concatenation.

Figure 3 shows the detailed structure of the regional U-Net used in Stage 2. The regional U-net receives eight consecutive slices centered on the slice predicted to have lung cancer in stage 1. Compared to the Global U-Net of Stage 1, the input size of the regional U-Net of Stage 2 is small. Therefore, in Stage 2, we designed a more sophisticated and complex network model, i.e., U-net, based on DenseNET [37].

We used  $2 \times 2$  max pooling with stride 2 for down-sampling to preserve the features between slices and dropout layers of 0.1 to prevent overfitting. The bridge section connecting the contracting and expansion paths comprised three convolution blocks to supplement a small retractive field of a  $3 \times 3 \times 3$  convolution layer. After 2D up-sampling, a  $3 \times 3 \times 3$  convolution layer reduces the number of channels that are equal to the number of channels being skipped.

**Fig. 3** Reginal 2.5D U-Net in Stage 2





**Fig. 4** A case of a 66-year-old male patient with lung cancer. (a) CT, (b) PET, (c) Ground truth, (d) Stage 1 output, and (e) Stage 2 output

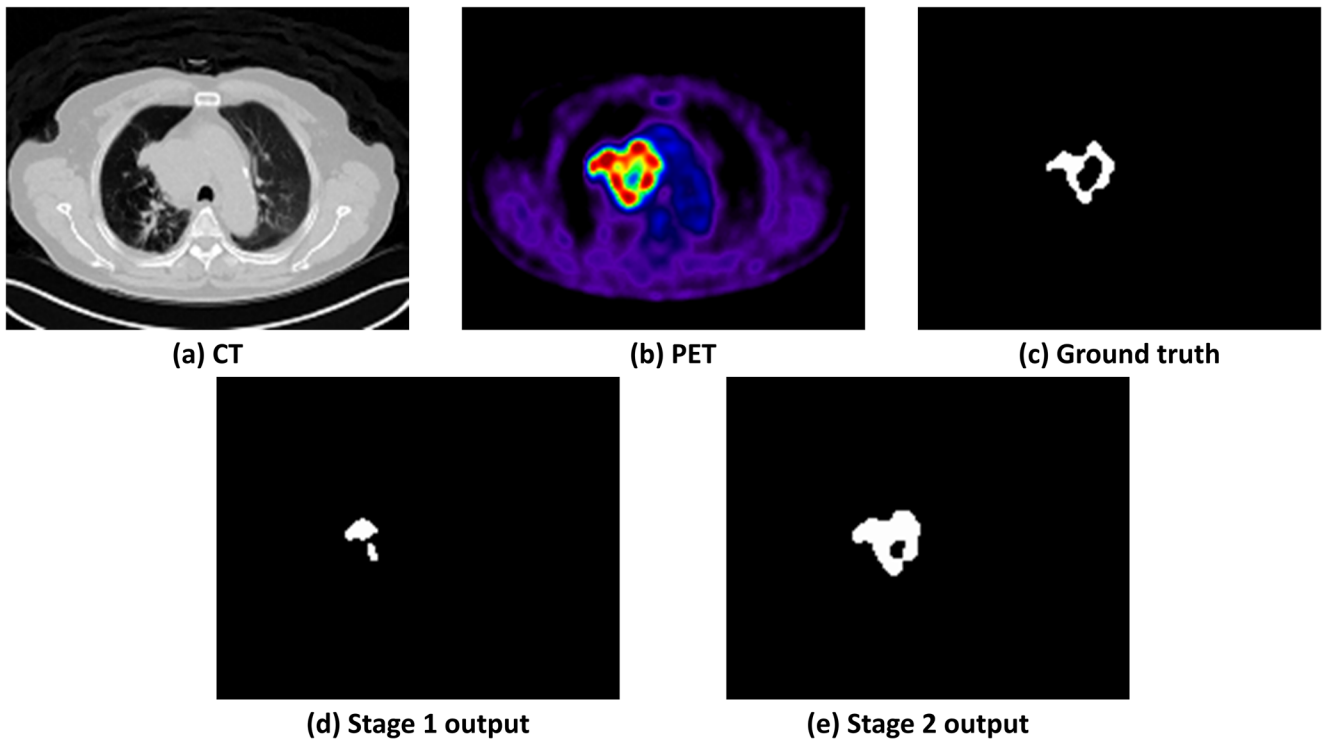


**Fig. 5** A case of a 77-year-old male patient with r/o lung cancer. (a) CT, (b) PET, (c) Ground truth, (d) Stage 1 output, and (e) Stage 2 output

**Table 1** Performance comparison between Stage 1 and Stage 2 U-Net approaches

Method	Mean Dice coefficient	Median Dice coefficient
1-Stage: Global U-Net only	0.74	0.86
2-Stage: Global + Regional U-Nets	0.78	0.90

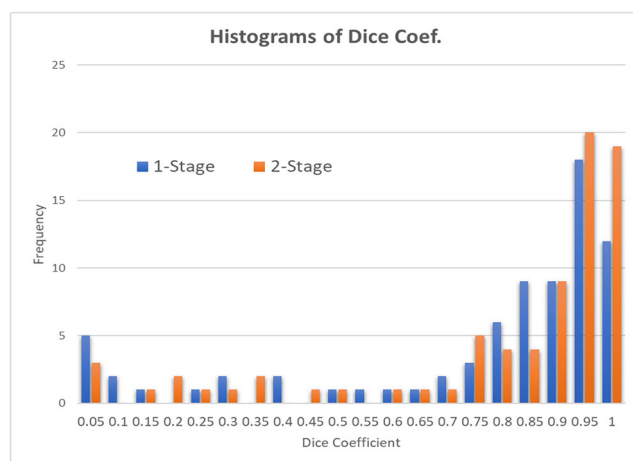
## Network Training and Evaluation

As a loss function for network training and performance indicator for network evaluation, we used the Dice similarity coefficient, which indicates the degree of overlap between the ground-truth and tumor regions segmented by deep neural networks.

Each model learns end-to-end mapping between the PET/CT images and VOI segmented by nuclear medicine physicians. Each layer was updated using error back-propagation with an adaptive moment estimation optimizer (ADAM), which is a stochastic optimization technique [38]. The exponential decay rates for the moment estimates  $\beta_1$  and  $\beta_2$  are 0.9 and 0.999, respectively, with  $\varepsilon = 10^{-8}$ .

The initial learning rate of the global U-Net was 0.1 and batch size was 6. The number of epochs was 45, and the learning rate was reduced by 0.1 times at 25 and 35 epochs. After the last sigmoid layer, we set the threshold to 0.6, which causes the validation set to lose its smallest value.

The initial learning rate of the regional U-Net was 0.001, and the batch size was 3. The number of epochs was 35, and the learning rate was reduced by half after every 5 epochs. After the last sigmoid layer, we set the threshold to 0.7, which causes the validation set to lose its smallest value.

**Fig. 6** Histograms of Dice coefficient for test set

## Results

As shown in Figs. 4 and 5, the two-stage U-Net architecture proposed in this study outperformed the conventional one-stage 3D U-Net (Global U-Net in Stage 1) in primary lung cancer segmentation. The detailed margin of tumors, determined by manually drawing spherical VOIs and applying an adaptive threshold, was well predicted by the two-stage U-Net model.

Quantitative analysis using the Dice similarity coefficient confirmed the advantages of the two-stage U-Net. The mean and median Dice similarity coefficients obtained by applying the one-stage and two-stage U-Net architectures are summarized in Table 1: The two-stage U-Net showed higher mean and median Dice similarity coefficients than those of the one-stage U-Net. It was observed that there is a difference  $> 0.1$  in mean and median Dice similarity coefficients. As shown in Fig. 6, in most cases, the proposed two-stage U-Net yielded a Dice similarity coefficient of 0.75 or greater. The Dice coefficient of 1-stage and 2-stage was significantly different with  $P$  value of 0.028 ( $< 0.05$ ) when paired  $t$ -test was performed.

Both methods take less than 1.5 s for data loading and segmentation. The difference in computation time was not significant.

## Discussion

Low standard uptake value (SUV) in lung cancer is the main cause of segmentation failure. Figure 7 shows an example of an unsuccessful lung cancer segmentation by the network. In this case, the maximum and mean SUVs in the lung cancer were only 1.00 and 0.75, respectively, and the global U-Net in Stage 1 could not detect the cancer. Table 2 shows the maximum and mean SUVs of three missed cases (Dice similarity coefficient = 0) by the two-stage U-Net, which are compared with the average maximum and mean SUVs of all cases in the test set. SUV level seems to mainly affect stage 1 (actually, zero output was obtained in five cases with low SUV), and stage 2 seems to contribute to finding more detailed

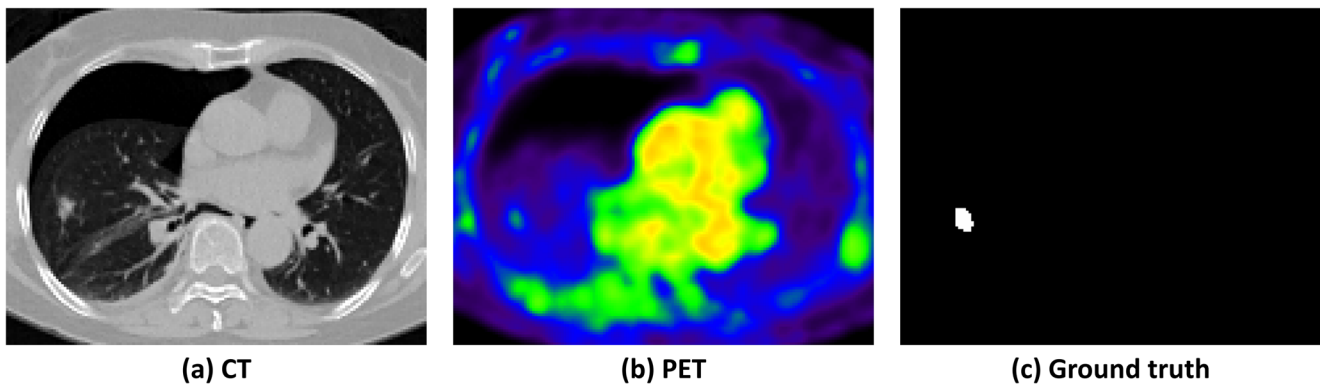


**Fig. 7** A false negative case. (a) CT, (b) PET, and (c) Ground truth

boundaries for tumor. The number of missed cases in 1-stage and 2-stage were five and three. In three cases, neither 1-stage nor 2-stage detected the tumors. In other two cases, 1-stage missed the tumor (Dice coefficient = 0), but 2-stage successfully segmented the tumors from the output slices of 1-stage.

Occasionally, the two-stage U-Net detected lymph nodes and distant metastases, although they were not included in the training set. Training networks with additional data with ground-truth segmentation of lymph nodes and distant metastasis are likely to enhance the usefulness of the proposed method.

One of the limitations of this study is that the final output of the proposed method a 2D slice rather than a 3D volume. This can lead to discontinuity of binary segments in coronal and sagittal slices.

There is room for further improvement in segmentation performance. In this study, only the usefulness of a 2-stage network was investigated. Further investigation to improve and optimize the network architecture will be necessary. Because lung cancer occupies a very small part of the body, small errors cause large degradation in DSC. Therefore, lung segmentation shows lower DSC compared to other segmentation tasks.

**Table 2** SUV means and standard deviations (STDs) of the cases with zero Dice coefficients

	Test set	Case 1	Case 2	Case 3
SUV mean	4.23	1.25	1.28	0.76
SUV STD	1.08	0.16	0.13	0.09

## Conclusion

In this study, we developed an automatic deep-learning-based [ $^{18}\text{F}$ ]FDG PET/CT lung cancer segmentation method. The proposed 2-Stage U-Net model achieves a Dice similarity coefficient of 0.78 for the test set. The proposed method will be useful for reducing the time and effort required for accurate lung cancer segmentation in [ $^{18}\text{F}$ ]FDG PET/CT.

**Author Contribution** The study was designed by Jun Young Park, Seung Kwan Kang, Donghwi Hwang, Jae Seon Eo, and Jae Sung Lee. Material preparation and data collection were performed by Hongyoon Choi, Seunggyun Ha, and Jae Seon Eo. The first draft of the manuscript was written by Jun Young Park, and Jae Sung Lee and all authors commented on previous versions of the manuscript. All authors read and approved the final manuscript.

**Funding** This research was supported by the Korea University Grant (K2119081) and the National Research Foundation of Korea (NRF) Grant funded by the Korea Government (MSIP) (No. 2018R1C1B5085202).

**Data Availability** Contact the corresponding author for data requests.

## Declarations

**Competing Interests** Jun Young Park, Seung Kwan Kang, Donghwi Hwang, Hongyoon Choi, Seunggyun Ha, Jong Mo Seo, Jae Seon Eo, and Jae Sung Lee declare no competing interests.

**Ethics Approval and Consent to Participate** The study was approved by the institutional review board of Seoul National University Hospital (H-2106-027-1225), and the requirement for written consent was waived by the institutional review board. All procedures performed in studies involving human participants were in accordance with the Helsinki Declaration as revised in 2013 and its later amendments.

**Consent for Publication** Not applicable.

## References

- Siegel RL, Miller KD, Jemal A. Cancer statistics, 2020. *CA Cancer J Clin.* 2020;70:7–30.
- Kandathil A, Kay FU, Butt YM, Wachsmann JW, Subramaniam RM. Role of FDG PET/CT in the eighth edition of TNM staging of non-small cell lung cancer. *Radiographics.* 2018;38:2134–49.
- Ettinger DS, Wood DE, Aisner DL, Akerley W, Bauman J, Chirieac LR, et al. Non-small cell lung cancer, version 5.2017, NCCN clinical practice guidelines in oncology. *J Natl Compr Cancer Netw.* 2017;15:504–35.
- Ravenel JG, Rosenzweig KE, Kirsch J, Ginsburg ME, Kanne JP, Kestin LL, et al. ACR Appropriateness Criteria non-invasive clinical staging of bronchogenic carcinoma. *J Am Coll Radiol.* 2014;11:849–56.
- Silvestri GA, Gonzalez AV, Jantz MA, Margolis ML, Gould MK, Tanoue LT, et al. Methods for staging non-small cell lung cancer: diagnosis and management of lung cancer, 3rd ed: American College of Chest Physicians evidence-based clinical practice guidelines. *Chest.* 2013;143:e211S–e50S.
- Khouani A, El Habib DM, Mahmoudi SA, Chikh MA, Benzineb B. Automated recognition of white blood cells using deep learning. *Biomed Eng Lett.* 2020;10:359–67.
- Lee JH, Kim YJ, Kim KG. Bone age estimation using deep learning and hand X-ray images. *Biomed Eng Lett.* 2020;10:323–31.
- Lee JS. A review of deep-learning-based approaches for attenuation correction in positron emission tomography. *IEEE Trans Radiat Plasma Med Sci.* 2020;5:160–84.
- Hwang D, Kim KY, Kang SK, Seo S, Paeng JC, Lee DS, et al. Improving the accuracy of simultaneously reconstructed activity and attenuation maps using deep learning. *J Nucl Med.* 2018;59:1624–9.
- Park J, Hwang D, Kim KY, Kang SK, Kim YK, Lee JS. Computed tomography super-resolution using deep convolutional neural network. *Phys Med Biol.* 2018;63:145011.
- Kang SK, Seo S, Shin SA, Byun MS, Lee DY, Kim YK, et al. Adaptive template generation for amyloid PET using a deep learning approach. *Hum Brain Mapp.* 2018;39:3769–78.
- Verma R, Mehrotra R, Rane C, Tiwari R, Agariya AK. Synthetic image augmentation with generative adversarial network for enhanced performance in protein classification. *Biomed Eng Lett.* 2020;10:443–52.
- Kim J-Y, Suh HY, Ryoo HG, Oh D, Choi H, Paeng JC, et al. Amyloid PET quantification via end-to-end training of a deep learning. *Nucl Med Mol Imaging.* 2019;53:340–8.
- Reader AJ, Corda G, Mehranian A, Cd C-L, Ellis S, Schnabel JA. Deep learning for PET image reconstruction. *IEEE Trans Radiat Plasma Med Sci.* 2021;5:1–25.
- Guo Z, Li X, Huang H, Guo N, Li Q. Deep learning-based image segmentation on multimodal medical imaging. *IEEE Trans Radiat Plasma Med Sci.* 2019;3:162–9.
- Borrelli P, Ly J, Kaboteh R, Ulén J, Enqvist O, Trägårdh E, et al. AI-based detection of lung lesions in [(18)F]FDG PET-CT from lung cancer patients. *EJNMMI Phys.* 2021;8:32.
- Hyun SH, Ahn MS, Koh YW, Lee SJ. A machine-learning approach using PET-based radiomics to predict the histological subtypes of lung cancer. *Clin Nucl Med.* 2019;44:956–60.
- Krarp MMK, Krokos G, Subesinghe M, Nair A, Fischer BM. Artificial intelligence for the characterization of pulmonary nodules, lung tumors and mediastinal nodes on PET/CT. *Semin Nucl Med.* 2021;51:143–56.
- Schwyzer M, Martini K, Benz DC, Burger IA, Ferraro DA, Kudura K, et al. Artificial intelligence for detecting small FDG-positive lung nodules in digital PET/CT: impact of image reconstructions on diagnostic performance. *Eur Radiol.* 2020;30:2031–40.
- Foster B, Bagci U, Mansoor A, Xu Z, Mollura DJ. A review on segmentation of positron emission tomography images. *Comput Biol Med.* 2014;50:76–96.
- Tau N, Stundzia A, Yasufuku K, Hussey D, Metser U. Convolutional neural networks in predicting nodal and distant metastatic potential of newly diagnosed non-small cell lung cancer on FDG PET images. *AJR Am J Roentgenol.* 2020;215:192–7.
- Ronneberger O, Fischer P, Brox T. (2015) U-net: convolutional networks for biomedical image segmentation. *Proc Med Image Comput Comput Assist Interv* 234–241.
- Park J, Bae S, Seo S, Park S, Bang JI, Han JH, et al. Measurement of glomerular filtration rate using quantitative SPECT/CT and deep-learning-based kidney segmentation. *Sci Rep.* 2019;9:4223.
- Park J, Lee JS, Oh D, Ryoo HG, Han JH, Lee WW. Quantitative salivary gland SPECT/CT using deep convolutional neural networks. *Sci Rep.* 2021;11:7842.
- Hegazy MAA, Cho MH, Cho MH, Lee SY. U-net based metal segmentation on projection domain for metal artifact reduction in dental CT. *Biomed Eng Lett.* 2019;9:375–85.
- Yie SY, Kang SK, Hwang D, Lee JS. Self-supervised PET denoising. *Nucl Med Mol Imaging.* 2020;54:299–304.
- Alom MZ, Yakopcic C, Hasan M, Taha TM, Asari VK. Recurrent residual U-Net for medical image segmentation. *J Med Imaging.* 2019;6:014006.
- Zhou Z, Siddiquee MMR, Tajbakhsh N, Liang J. Unet++: a nested u-net architecture for medical image segmentation. *Lect Notes Comput Sci.* 2018;11045:3–11.
- Choi B-H, Hwang D, Kang S-K, Kim K-Y, Choi H, Seo S, et al. Accurate transmission-less attenuation correction method for amyloid- $\beta$  brain PET using deep neural network. *Electronics.* 2021;10:1836.
- Çiçek Ö, Abdulkadir A, Lienkamp SS, Brox T, Ronneberger O. (2016) 3D U-Net: learning dense volumetric segmentation from sparse annotation. *Proc Med Image Comput Comput Assist Interv* 424–32.
- Na KJ, Choi H, Oh HR, Kim YH, Lee SB, Jung YJ, et al. Reciprocal change in glucose metabolism of cancer and immune cells mediated by different glucose transporters predicts immunotherapy response. *Theranostics.* 2020;10:9579–90.
- Nioche C, Orhac F, Boughdad S, Reuzé S, Goya-Outi J, Robert C, et al. LIFEx: a freeware for radiomic feature calculation in multimodality imaging to accelerate advances in the characterization of tumor heterogeneity. *Cancer Res.* 2018;78:4786–9.
- Nestle U, Kremp S, Schaefer-Schuler A, Sebastian-Welsch C, Hellwig D, Rube C, et al. Comparison of different methods for delineation of 18F-FDG PET-positive tissue for target volume definition in radiotherapy of patients with non-small cell lung cancer. *J Nucl Med.* 2005;46:1342–8.
- Hwang D, Kang SK, Kim KY, Choi H, Seo S, Lee JS. Data-driven respiratory phase-matched PET attenuation correction without CT. *Phys Med Biol.* 2021. <https://doi.org/10.1088/1361-6560/abfc8f>.
- Hwang D, Kang SK, Kim KY, Seo S, Paeng JC, Lee DS, et al. Generation of PET attenuation map for whole-body time-of-flight (18)F-FDG PET/MRI using a deep neural network trained with simultaneously reconstructed activity and attenuation maps. *J Nucl Med.* 2019;60:1183–9.

36. Lee MS, Hwang D, Kim JH, Lee JS. Deep-dose: a voxel dose estimation method using deep convolutional neural network for personalized internal dosimetry. *Sci Rep*. 2019;9:10308.
37. Wang C, Zhao Z, Ren Q, Xu Y, Yu Y. Dense U-net based on patch-based learning for retinal vessel segmentation. *Entropy*. 2019;21:168.
38. Kingma DP, Ba J. Adam: a method for stochastic optimization. San Diego: Proceedings of the 3rd International Conference on Learning Representations; 2015. p. 7–9.

**Publisher's Note** Springer Nature remains neutral with regard to jurisdictional claims in published maps and institutional affiliations.

## Affiliations

Junyoung Park<sup>1,2</sup> · Seung Kwan Kang<sup>2,3,4,5</sup> · Donghwi Hwang<sup>2,3,4</sup> · Hongyoon Choi<sup>2</sup> · Seunggyun Ha<sup>6</sup> · Jong Mo Seo<sup>1</sup> · Jae Seon Eo<sup>7</sup> · Jae Sung Lee<sup>2,3,4,5,8</sup> 

Junyoung Park  
parkjun210@snu.ac.kr

Seung Kwan Kang  
kevin.kang@brtnx.com

Donghwi Hwang  
hwang0310@snu.ac.kr

Hongyoon Choi  
chy1000@gmail.com

Seunggyun Ha  
seunggyun.ha@gmail.com

Jong Mo Seo  
callme@snu.ac.kr

<sup>1</sup> Department of Electrical and Computer Engineering, Seoul National University College of Engineering, Seoul 08826, Korea

<sup>2</sup> Department of Nuclear Medicine, Seoul National University College of Medicine, 103 Daehak-ro, Jongno-gu, Seoul 03080, Korea

<sup>3</sup> Department of Biomedical Sciences, Seoul National University College of Medicine, Seoul 03080, Korea

<sup>4</sup> Artificial Intelligence Institute, Seoul National University, Seoul 08826, Korea

<sup>5</sup> Brightonix Imaging Inc., Seoul 03080, Korea

<sup>6</sup> Division of Nuclear Medicine, Department of Radiology, Seoul St Mary's Hospital, The Catholic University of Korea, Seoul 06591, Korea

<sup>7</sup> Department of Nuclear Medicine, Korea University Guro Hospital, 148 Gurodong-ro, Guro-gu, Seoul 08308, Korea

<sup>8</sup> Institute of Radiation Medicine, Medical Research Center, Seoul National University College of Medicine, Seoul 03080, Korea